Since January 2020 Elsevier has created a COVID-19 resource centre with free information in English and Mandarin on the novel coronavirus COVID-19. The COVID-19 resource centre is hosted on Elsevier Connect, the company's public news and information website.

Biomaterials 291 (2022) 121898

Contents lists available at ScienceDirect

Biomaterials

journal homepage: www.elsevier.com/locate/biomaterials

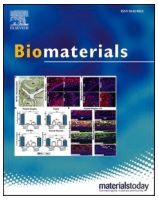

Self-cleaning wearable masks for respiratory infectious pathogen inactivation by type I and type II AIE photosensitizer

Jingxuan Sun [a,1], Yujie Bai [a,1], Eric Y. Yu [b,1], Guanyu Ding [c], Haili Zhang [a], Ming Duan [a], Pei Huang [a], Mengyao Zhang [a], Hongli Jin [a], Ryan TK. Kwok [b], Yuanyuan Li [a,*], Guo-Gang Shan [c,**], Ben Zhong Tang [d,***], Hualei Wang [a,****]

[a] Key Laboratory of Zoonosis Research, Ministry of Education, College of Veterinary Medicine, Jilin University, Changchun, China
[b] Department of Chemistry, Hong Kong Branch of Chinese National Engineering Research Center for Tissue Restoration and Reconstruction, The Hong Kong University of Science and Technology, Clear Water Bay, Kowloon, China
[c] Institute of Functional Material Chemistry and National & Local United Engineering Lab for Power Battery, Faculty of Chemistry, Northeast Normal University, Changchun, 130024, China
[d] School of Science and Engineering, Shenzhen Institute of Aggregate Science and Technology, The Chinese University of Hong Kong, Shenzhen, Guangdong, 518172, China

ARTICLE INFO

Keywords:
Personal protective equipment
Photosensitizer
Influenza A virus
Streptococcus pneumoniae
Aggregation-induced emission
Sunlight inactivation

ABSTRACT

Although face masks as personal protective equipment (PPE) are recommended to control respiratory diseases with the on-going COVID-19 pandemic, improper handling and disinfection increase the risk of cross-contamination and compromise the effectiveness of PPE. Here, we prepared a self-cleaning mask based on a highly efficient aggregation-induced emission photosensitizer (TTCP-PF_6) that can destroy pathogens by generating Type I and Type II reactive oxygen species (ROS). The respiratory pathogens, including influenza A virus H1N1 strain and *Streptococcus pneumoniae* (*S. pneumoniae*) can be inactivated within 10 min of ultra-low power (20 W/m^2) white light or simulated sunlight irradiation. This TTCP-PF_6-based self-cleaning strategy can also be used against other airborne pathogens, providing a strategy for dealing with different microbes.

1. Introduction

Severe acute respiratory syndrome coronavirus 2 (SARS-CoV-2) has caused many infections and deaths [1–5], thereby preventing the spread of respiratory pathogens, including viruses, bacteria, mycoplasmas, and chlamydia has gained lots of attention. The use of personal protective equipment (PPE), such as face masks, has been highly recommended to prevent the transfer of respiratory pathogens since the dominant from of transmission is through pathogens-containing respiratory droplets and direct physical contact [6–9]. However, pathogens can survive and accumulate on the surface of masks, and prolonged or repeated usage of single-use masks increases the risk of infection to the wearer [10]. Therefore, effective use of PPE includes changing masks timely and removing and discarding masks properly to prevent physical exposure. Improper disposal of used masks outside the healthcare environment may pose a high risk of cross-contamination and expose the wearer and other people to re-transmission of infectious pathogens [11,12]. Therefore, there is an urgent need to exploit PPE with reusable, broad-spectrum inactivation and easy to sterile abilities.

Self-cleaning PPE has been recently developed for disinfection based on photothermal or photodynamic strategies. Although most infectious microbes can be inactivated under photothermal effects, the use of high temperatures will not only result in discomfort to the wearer but also pose potential fire risks and other safety concerns [13,14]. Alternatively, self-sterilization by photodynamic strategy may address these limitations as photodynamic-based masks can generate reactive oxygen species (ROS) that can rapidly destroy proteins, nucleic acids, and lipids of pathogens without any heat generated [15–20]. ROS mainly includes

* Corresponding author.
** Corresponding author.
*** Corresponding author.
**** Corresponding author.
E-mail addresses: li_yuanyuan@jlu.edu.cn (Y. Li), shangg187@nenu.edu.cn (G.-G. Shan), tangbenz@cuhk.edu.cn (B.Z. Tang), wanghualei@jlu.edu.cn (H. Wang).
[1] These authors contributed equally: Jingxuan Sun, Yujie Bai, Eric Y. Yu.

https://doi.org/10.1016/j.biomaterials.2022.121898
Received 20 August 2022; Received in revised form 23 October 2022; Accepted 30 October 2022
Available online 10 November 2022

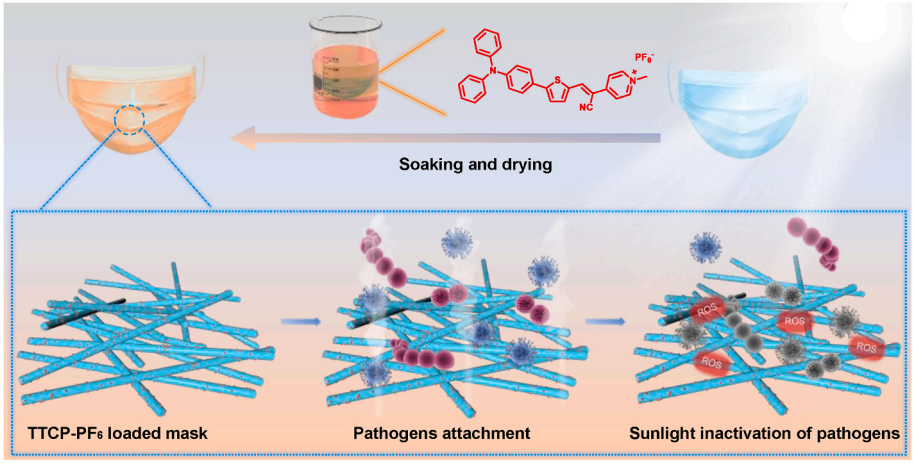

Scheme 1. The photodynamic inactivation mechanism of TTCP-PF_6 against pathogens upon sunlight irradiation.

Type I ROS (superoxide anion radical (O_2• -), and hydroxyl radical (•OH)) and Type II ROS (singlet oxygen, ($^1O_2$)) [21]. A handful of photosensitizers (PSs) have been reported to produce $^1O_2$, showing antimicrobial ability, but they rely heavily on oxygen availability and have a relatively short half-life of 10^{-5} s and diffusion distance of 2–3.5 mm in the air [18,22,23]. Compared to Type II ROS, O_2• - exhibit a much longer half-life (few seconds), and •OH radicals have been considered the most potent oxidizing species for the inactivation of microbes [21,24–27]. Thus, developing PSs capable of producing O_2• - and the highly toxic •OH as antimicrobial agents is a plus.

As one of the most advanced PSs, aggregation-induced emission photosensitizers (AIE PSs) have received great attention due to their inherent advantages of high efficiency, good photostability, and excellent biocompatibility [28–32]. Precise molecular design by tuning the π-conjugation and electron donor-acceptor (D-A) moiety allowed AIE luminogens (AIEgens) to possess both Type I and Type II ROS generation abilities [33–35]. And the aggregation-induced intersystem crossing (AI-ISC) mechanism [36,37] has made AIE PSs more efficient in ROS generation in their aggregate state, which is pivotal for photodynamic-based masks. Given the high market demand for face masks, cost reduction and simplification of the manufacturing processes are critical in a practical aspect and market commercialization of PPE [38–40]. Thus, developing PPE with excellent biocidal ability that is simple for mass production is very attractive.

Here, a new self-cleaning PPE (mask) with broad-spectrum antimicrobial capabilities based on TTCP-PF_6 was fabricated through a simple soaking and drying process (Scheme 1). TTCP-PF_6 served as a PS for its strong type I and type II ROS generation and is easily synthesized. As a proof of concept, influenza A virus H1N1 strain (IAV) and *Streptococcus pneumoniae* (*S. pneumoniae*) were utilized as respiratory pathogen models [41]. When IAV or *S. pneumoniae* -laden droplets get transferred onto the fibers of the TTCP-PF_6-loaded mask, massive ROS can be produced to inactivate the pathogen by optical sunlight simulator or ultra-low light irradiation, thus providing a basis for daily mask self-cleaning without the need for additional equipment. The TTCP-PF_6-based mask can fight against airborne pathogens and holds great potential to reduce environmental pollution caused by the massive disposal of single-use masks and to aid the prevention of re-transmission.

2. Materials and method

2.1. Materials

Dulbecco's Modified Essential Medium (DMEM) was purchased from Corning (USA), fetal bovine serum (FBS) was purchased from Biological Industries (Israel), penicillin-streptomycin (SP) was purchased from HyClone (USA), Dimethyl sulfoxide (DMSO) was purchased from Sigma-Aldrich (USA). Surgical masks were purchased from FULANG (China). Influenza A H1N1 (A/WSN/1933, H1N1/WSN) was kept by our laboratory. *Streptococcus pneumoniae* (*S. pneumoniae*) was purchased from China General Microbiological Culture Collection Center (CGMCC).

Normal Madin-Darby canine kidney (MDCK) cells, normal human non-small cell lung cancer cells (A549), and normal human skin fibroblast cell line (HSF) cells were cultured in DMEM medium containing 10% FBS and 1% SP at 37 °C in a humidified incubator with 5% CO_2. All cells were cultured in 25 cm^2 cell culture flasks (Corning, USA).

Six-week-old female ICR mice were performed under the protocol of the Scientific Ethics Committee of Jilin University (SY202207008).

2.2. Characterization

^1H and ^{13}C HMR spectra were measured on a 500 MHz Bruker Avance spectrometer using $CDCl_3$ or DMSO-d_6 as the deuterium solvent and tetramethylsilane (TMS; $\delta = 0$ ppm) was selected as the internal reference. High-resolution mass spectra (HRMS) were documented on matrix-assisted laser desorption ionization time-of-flight (MALDI-TOF) mass spectrometer. UV–vis absorption spectra were recorded on Cary 500 UV–vis–NIR spectrophotometer. Steady-state fluorescence spectra were recorded on FL-4600 fluorescent spectrophotometer. The structure of blank fabrics and TTCP-PF_6 was examined with a field emission scanning electron microscope (FESEM, S4800, Hitachi Co., Japan).

2.3. Preparation and characterization of mask-TTCP-PF_6

Mask-TTCP-PF_6 was prepared by the soaking and solvent evaporation process. TTCP-PF_6 was first dissolved in PBS to prepare a TTCP-PF_6 solution at a concentration of 2 μM. Next, the original fabric of the surgical mask was cut into 1 cm × 1 cm and placed directly into the TTCP-PF_6 solution and soaked at room temperature until the fabric was completely dyed and then dried at room temperature thermostat. The ratio of fabric to TTCP-PF_6 solution (liquid ratio) was controlled from 1:30 to 1:50. Scanning electron microscopy (SEM) images were captured to ensure that TTCP-PF_6 adhered to the fabric.

2.4. Measurement of ROS produced by TTCP-PF_6 and TTCP-PF_6-loaded mask

Choosing 2′,7′-dichlorodihydrofluorescein diacetate (DCFH-DA), 9,10-anthracenediyl-bis(methylene) dimalonic acid (ABDA), hydroxyphenyl fluorescein (HPF), dihydrorhodamine 123 (DHR123) as indicators for ROS, $^1O_2$, •OH radicals, and $O_2^{\bullet}$ - measurement, respectively. A stock solution of ABDA was diluted to 50 μM in a water

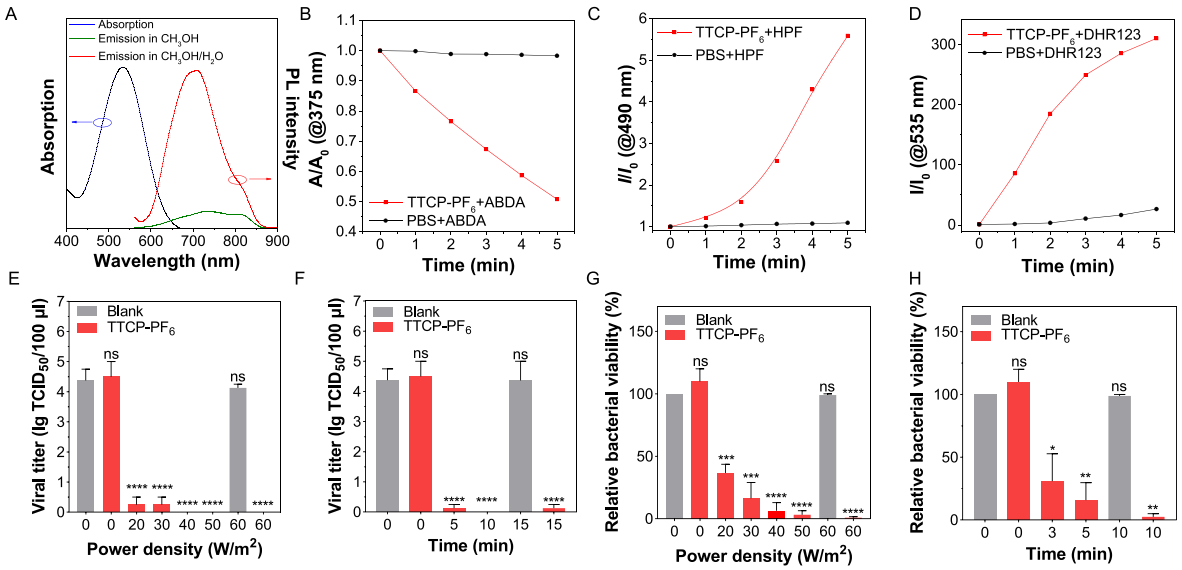

Fig. 1. Characterization and anti-pathogenic efficiency of TTCP-PF$_6$. (A) The normalized absorption spectrum and PL spectra of TTCP-PF$_6$ in the solution (methanol) or aggregate (methanol/H_2O = 1:9) state. (B) ABDA is the indicator for $^1O_2$ (C) HPF is the indicator for •OH. (D) DHR123 is the indicator for $O_2^{\bullet-}$; (E) Virus titer of H1N1/WSN with 2 μM TTCP-PF$_6$ followed by 5 min white light illumination with different power densities. (F) Virus titer of H1N1/WSN with 2 μM TTCP-PF$_6$ followed by 20 W/m^2 white light irradiation for different durations. (G) Relative bacterial viability of *S. pneumoniae* with 2 μM TTCP-PF$_6$ followed by 5 min white light irradiation with different power densities. (H) Relative bacterial viability of *S. pneumoniae* with 2 μM TTCP-PF$_6$ followed by 20 W/m^2 white light irradiation for different durations.

solution containing 2 μM of TTCP-PF$_6$. The solution was irradiated by white light (100 W/m^2) at 1 min intervals. After irradiation and thorough mixing, the absorption spectra were measured one by one to record the degradation of ABDA.

TTCP-PF$_6$-loaded or the original fabric (1 cm × 1 cm) was immersed in 2 mL of 50 μM ABDA solution in a glass Petri dish. Then, the samples were exposed to a LED light at a density of 100 W/m^2 for different durations. The degradation of ABDA in the solution is caused by the quenching of the single linear oxygen ($^1O_2$) and can be detected at the indicated times using a UV–Vis spectrophotometer. The maximum absorption intensity of ABDA at a wavelength of 378 nm was recorded and the concentration of ABDA solution before and after light exposure was calculated. The change in concentration of ABDA (ΔC-ABDA) was used to evaluate the $^1O_2$ produced by TTCP-PF$_6$.

The stock solution of DCFH (10 mM in DMSO) was diluted to 10 μM in a water solution containing 2 μM of TTCP-PF$_6$. The solution was irradiated by white light (100 W/m^2) at 1 min intervals. After irradiation and thorough mixing, the emission spectra were measured one by one with excitation at 488 nm, and emission was collected from 488 to 525 nm.

The stock solution of HPF (5 mM in DMF) was diluted to 10 μM in a water solution containing 2 μM of TTCP-PF$_6$. The solution was irradiated by white light (100 W/m^2) at 1 min intervals. After irradiation and thorough mixing, the emission spectra were measured one by one with excitation at 480 nm and emission collected from 490 to 600 nm.

The stock solution of DHR 123 (10 mM in DMSO) was diluted to 10 μM in a water solution containing 2 μM of TTCP-PF$_6$. The solution was irradiated by white light (100 W/m^2) at 10 s intervals. After irradiation and thorough mixing, the emission spectra were measured one by one with excitation at 490 nm and emission collected from 500 to 650 nm.

2.5. Photostability tests of TTCP-PF$_6$

The prepared Mask-TTCP-PF$_6$ was continuously irradiated under a white light of 20 W/m^2 density for 2 h. The ROS generation ability and the structure of Mask-TTCP-PF$_6$ were assessed and compared with unirradiated Mask-TTCP-PF$_6$.

2.6. Washability tests of TTCP-PF$_6$

The Mask-TTCP-PF$_6$ (1 cm × 1 cm) was placed in a centrifuge tube containing 5 mL of deionized water and stirred at 200 rpm for 10 min at room temperature. The Mask-TTCP-PF$_6$ was then transferred to another new centrifuge tube containing 5 mL of deionized water and washed repeatedly. After 100 times washing, the Mask-TTCP-PF$_6$ was allowed to dry naturally. The ROS generation ability and the structure of Mask-TTCP-PF$_6$ were assessed and compared with unwashed Mask-TTCP-PF$_6$.

2.7. The anti-pathogenic effect of TTCP-PF$_6$

10^4 TCID$_{50}$/100 μL of H1N1/WSN or 10^7 CFU/mL of *S. pneumoniae* was mixed directly with TTCP-PF$_6$. The mixture was then placed under white light irradiation with a density of 20 W/m^2 for different durations or under white light irradiation for 5 min with different power densities.

The residual viruses [42] and bacteria [43] were measured according to standard protocols in the previously reported articles. Briefly, 100 μL of H1N1/WSN dilution was added to the MDCK cell in 96-wells after serial dilution and incubated for 48 h at 37 °C to determine TCID$_{50}$ by the method of Reed and Muench. And 20 μL of *S. pneumoniae* dilution was spread onto a non-resistant LB plate and incubated at 37 °C to calculate the colony counts of *S. pneumoniae*.

2.8. The anti-pathogenic effect of mask-TTCP-PF$_6$

H1N1/WSN suspension with 10^7 TCID$_{50}$/100 μL or 10^5 TCID$_{50}$/100 μL, or *S. pneumoniae* suspension with 10^7 CFU/mL or 10^5 CFU/mL uniformly sprayed on the surface for Mask-TTCP-PF$_6$ or control fabrics in a size of 1 cm × 1 cm. The fabrics were exposed to white light at a density of 20 W/m^2 for different durations. At each specific time point of illumination, the fabrics were immersed in 500 μL of DMEM/LB to collect residual H1N1/WSN or *S. pneumoniae* from the fabrics.

2.9. Cell viability study

CCK-8 assay was used to evaluate the cytotoxicity of TTCP-PF$_6$. HSF cells were seeded in 96-well plates (Corning, USA) at a density of 1.5 ×

10^4 cells/mL, and A549 cells were seeded in 96-well plates at a density of 1×10^4 cells/mL and incubated at 37 °C. After overnight incubation, the medium of each well was replaced with 100 μL of fresh medium containing different concentrations of TTCP-PF_6 with 5 replicates of each test group. After 24 h of treatment, 10 μL CCK8 (ApexBio, USA) was added to each well. After 1 h, absorbance (OD) was measured at 450 nm in a microplate reader (Biotek, USA). Cell viability was determined by the ratio of the absorbance of the TTCP-PF_6-treated cell group to the absorbance of the untreated cell group.

2.10. Long-term toxicity assay in vivo

Different concentrations of TTCP-PF_6 were intranasally administrated or applied to the skin of mice. Mice in different groups were monitored and weighed daily. On the fifth day, the mice were executed, blood was collected, and vital organs and skin sections were separated. Blood samples were used for blood index and biochemical indexes testing. Vital organs and skin were fixed in 4% paraformaldehyde, then embedded in paraffin and sectioned 5 μm thick. Sections were stained with hematoxylin-eosin (HE) and imaged by light microscopy.

2.11. Statistical analysis

Quantitative data were expressed as mean ± SEM. Sample size (n) = 3 for each group. Statistical comparisons between two groups were determined by paired two-tailed *t*-test. Statistical comparisons among different groups (≥3) were determined by one-way ANOVA followed by a post-hoc Tukey's HSD test, and p values between each group were adjusted by Bonferroni correction. For all tests, $p < 0.05$ was considered statistically significant; *, **, and *** indicate $p < 0.05$, $p < 0.01$ and $p < 0.001$, respectively. All statistical calculations were performed using GraphPad Prism 8.0 Software, including assumptions of tests used (GraphPad Software Inc., CA, USA).

3. Results and discussion

3.1. Preparation and characterization of TTCP-PF_6

Here, TTCP-PF_6 with typical D-A skeletons was facilely synthesized by Knoevenagel condensation reaction between aldehyde intermediates and 2-(pyridin-4-yl) acetonitrile (Scheme S1) [44–46]. The structure of TTCP-PF_6 and other involved molecules was characterized with satisfactory results in the Supporting Information. The optical properties of TTCP-PF_6 were investigated by UV–vis and photoluminescence (PL) spectroscopies. As shown in Fig. 1A, the absorption spectral peak of TTCP-PF_6 in methanol was centered at 525 nm with a broad absorption, which is conducive to absorbing more sunlight. Moreover, it displayed AIE property, as proved by its enhanced PL intensity in MeOH/water mixtures with high water fractions (Figure S1). TTCP-PF_6 is expected to produce ROS in the aggregate states due to the promoted energy transfer between the lowest excited singlet state (S_1) and the lowest triplet state (T_1) caused by the prohibition of energy dissipation through non-radiative channels. The $^1O_2$, •OH radicals, and O_2• - generation abilities of TTCP-PF_6 were evaluated by ABDA, HPF, and DHR123, respectively [47–49]. The results in Fig. 1B–D revealed that both type I and type II ROS are produced by TTCP-PF_6 under ultra-low light irradiation, providing sufficient lifetime and diffusion distance to achieve a strong interaction with pathogens.

The wide range of ROS types and high generation efficiency prompted us to test its photodynamic inactivation (PDI) effect against pathogens alone in vitro. H1N1/WSN and *S. pneumoniae* were chosen as respiratory viruses and bacteria models, respectively. H1N1/WSN is one of the most common causes of respiratory infections [50–52], and *S. pneumoniae* has been identified as a predominant pathogen in secondary pneumonia cases [41,53]. After mixing H1N1/WSN or *S. pneumoniae* with TTCP-PF_6 aggregates, the viability of viruses and bacteria dropped rapidly with increased light density. The virus titer was reduced to about 90% under 20 W/m^2 white light irradiation for 5 min and became completely inhibited when increasing the power density to 40 W/m^2 or above (Fig. 1E–F). In the case of *S. pneumoniae*, approximately 50% of bacteria were killed after 3 min of light irradiation with a power density of 20 W/m^2 and almost complete bacterial inactivation in 10 min of irradiation (Fig. 1G–H). Meanwhile, the TTCP-PF_6 exhibited negligible dark toxicity to *S. pneumoniae* (Figure S3). These results indicate that TTCP-PF_6 possesses tremendous PDI effects against H1N1/WSN and *S. pneumoniae*. The low dosage benefits in cost savings for mass production, while the low light density and short irradiation time advocate a fast and persistent antimicrobial efficiency under both sunlight and indoor light irradiation.

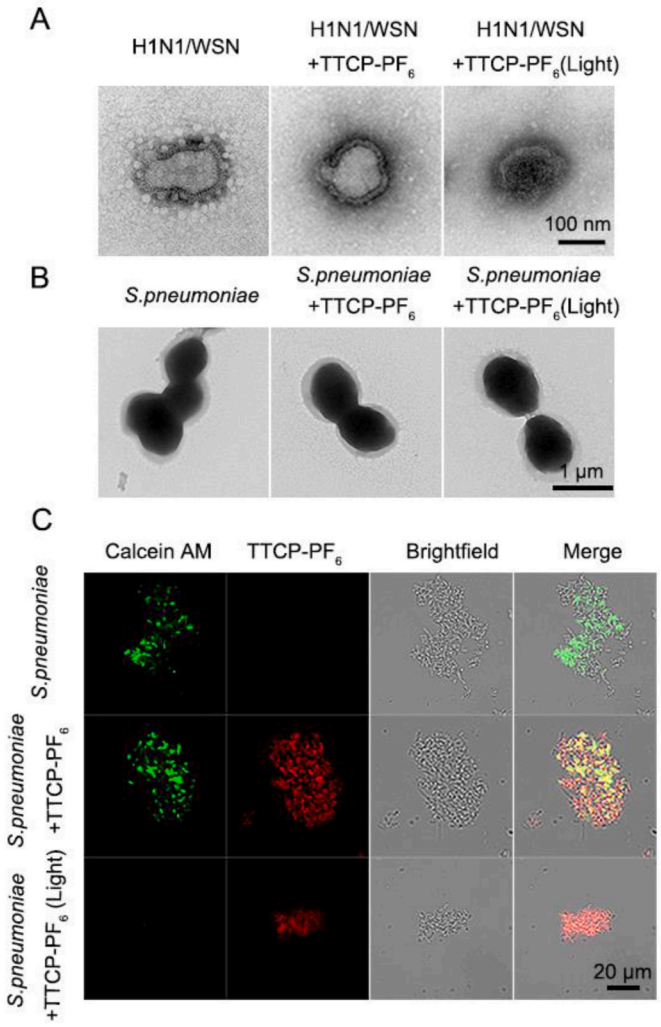

Fig. 2. Anti-pathogenic effect of TTCP-PF_6. (A) Morphology of H1N1/WSN with different treatments. (B) Morphology of *S. pneumoniae* after different treatment. (C) Live *S. pneumoniae* staining with different treatments.

To further verify the anti-pathogenic ability, the morphology of pathogens was evaluated by transmission electron microscopy (TEM) and the live status of bacteria was distinguished by confocal laser scanning microscopy (CLSM). As shown in Fig. 2A, in the absence of TTCP-PF_6 or TTCP-PF_6 without light irradiation, the morphology of H1N1/WSN remained intact and exhibited a clear envelope with visible vesicle protrusions. However, the morphology of H1N1/WSN showed evident disruption after treating with TTCP-PF_6 with light irradiation. Similar to viruses, bacteria were also shown obvious morphological changes. In the absence of TTCP-PF_6 or TTCP-PF_6 without light irradiation, the morphology of *S. pneumoniae* remained intact showing clear

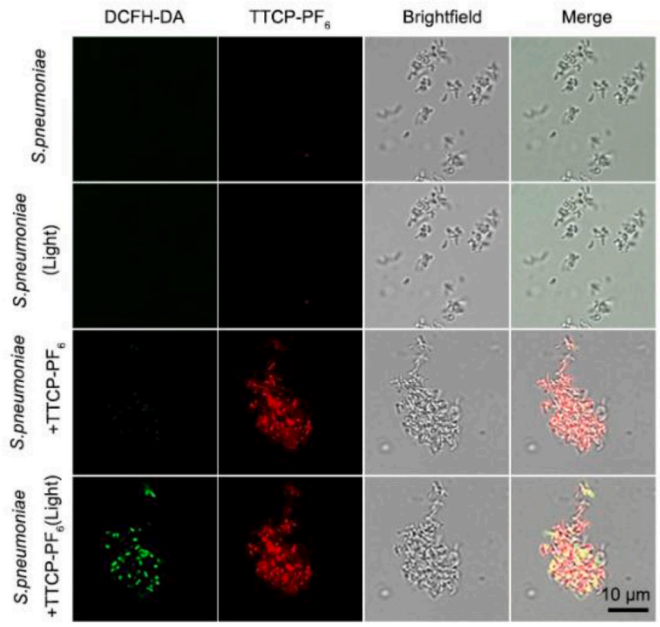

Fig. 3. Intracellular ROS of TTCP-PF_6 in *S. pneumoniae* was detected by DCFH-DA with various treatments.

envelope and chain structure. However, the morphology of *S. pneumoniae* showed evident disruption after treating with TTCP-PF_6 with light irradiation (Fig. 2B). Meanwhile, the live bacterial straining by calcein-AM showed that *S. pneumoniae* without TTCP-PF_6 and *S. pneumoniae* with TTCP-PF_6 in dark exhibited green fluorescence [54]. The red fluorescence of *S. pneumoniae* treated with TTCP-PF_6 can be clearly observed benefiting from the strong electrostatic interaction between the positive charged TTCP-PF_6 and the negative charged bacterial cell envelope. However, *S. pneumoniae* treated with TTCP-PF_6 and light irradiation only showed red fluorescence. All these results demonstrated that TTCP-PF_6 exhibited good performance for both virus and bacteria killing.

Further study on the potential anti-pathogen mechanisms was performed by evaluating intracellular ROS inside microenvironment of pathogens. Typically, massive production of endogenous ROS help induces high membrane permeability and other physiological disorders of pathogens [18,55–57]. 2′,7′-dichlorodihydrofluorescein diacetate (DCFH-DA) probe is a ROS tracker used frequently to evaluate endogenous ROS levels [58]. Bacterial capsule was negatively charged and can electrostatically interact with the positive charged TTPC-PF_6. As shown in Fig. 3, the absence of TTCP-PF_6 or TTCP-PF_6 without light irradiation showed negligible green fluorescence, while prominent green signals were observed in the group of *S. pneumoniae* treated with TTCP-PF_6 and light irradiation. This indicated that TTCP-PF_6 could produce ROS in pathogens rapidly and effectively under light irradiation. The influenza H1N1 virus is an enveloped virus consisting of negative charge envelope, which can be electrostatically interacted with positive charged TTCP-PF_6 as well.

3.2. Preparation, characterization, and stability tests of mask-TTCP-PF_6

Motivated by the capability of TTCP-PF_6 to provide a broad-spectrum resistance to different pathogenic microbes, we then pursued the fabrication of masks that were expected to be available for bioprotective devices. The TTCP-PF_6 loaded mask was prepared through a simple soaking and solvent evaporation process. The organization and physical properties of Mask-TTCP-PF_6 were systematically

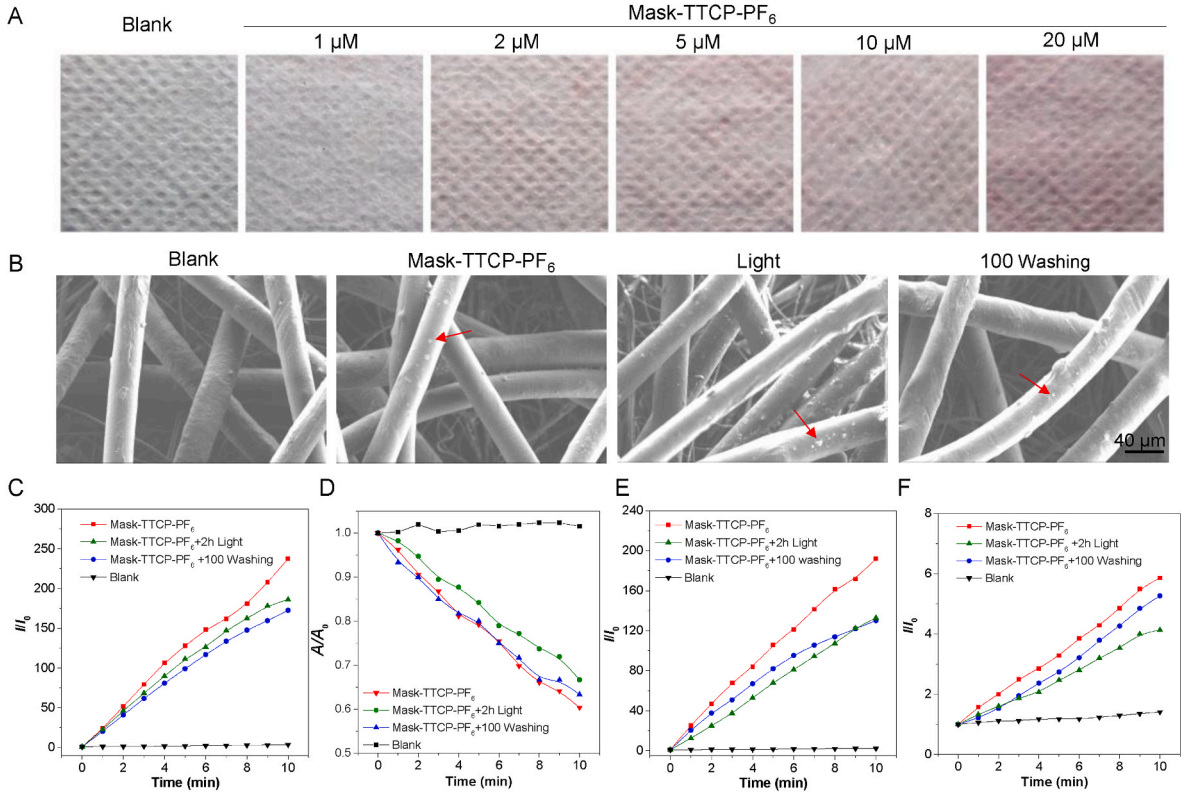

Fig. 4. Preparation, characterization, and washability tests of Mask-TTCP-PF_6. (A) Optical images of the blank fabrics, and newly prepared Mask-TTCP- PF_6. (B) SEM images of the blank fabrics, newly prepared Mask-TTCP-PF_6, Mask-TTCP- PF_6 after 2 h of lighting, and Mask-TTCP-PF_6 after 100 times of washing (arrows: TTCP-PF_6). Scale bars: 40 μm. The ROS (C), $^1O_2$ (D), •OH (E) and $O_2^{\bullet}$ - (F)generation ability of mask with different treatment using DCFH, ABDA, HPF and DHR 123 as the indicator respectively.

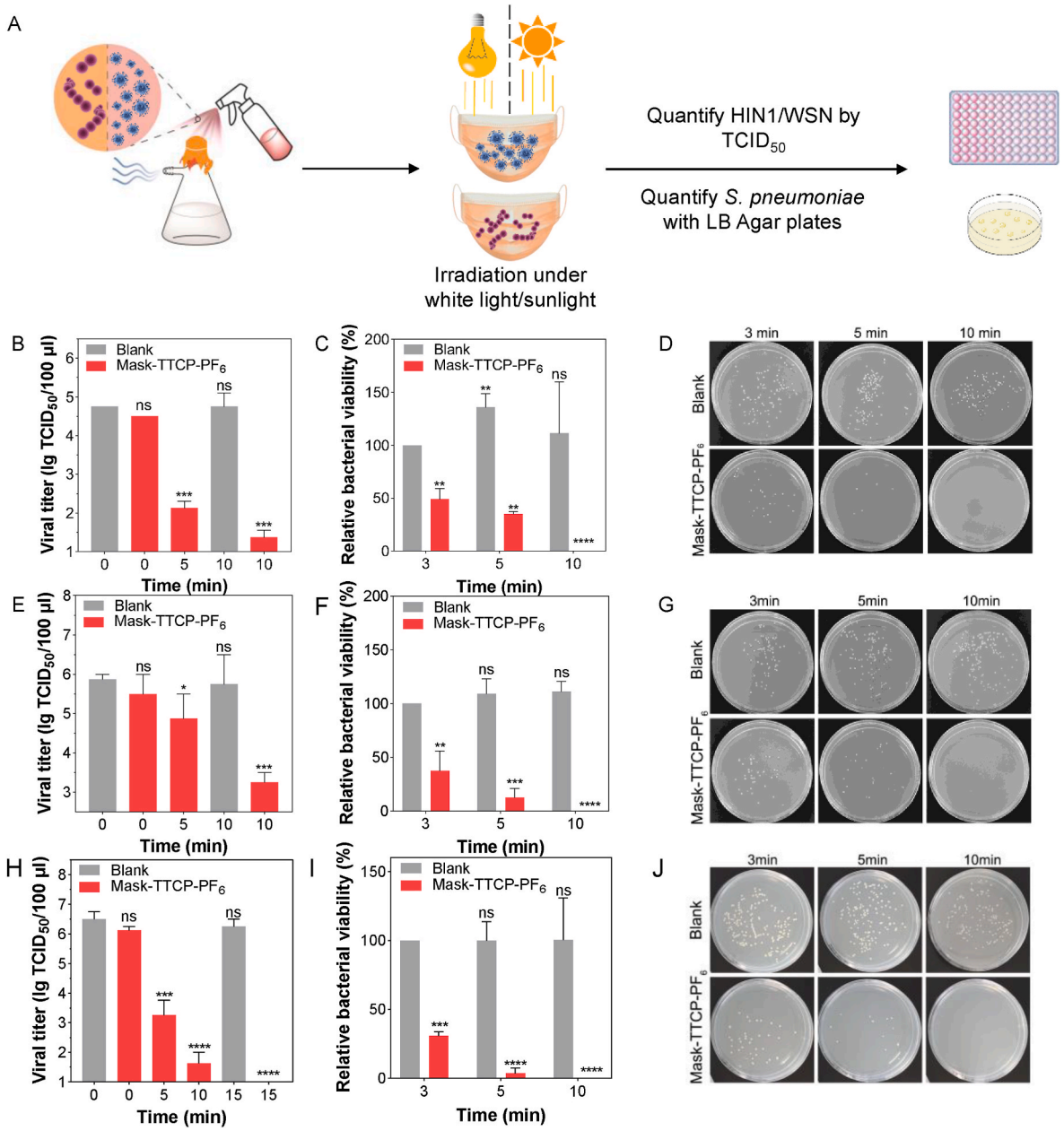

Fig. 5. Light-induced anti-pathogenic effect of Mask-TTCP-PF$_6$. (A) Schematic illustration of setup used to simulate the process of Mask-TTCP-PF$_6$ catching pathogens-laden aerosols in practical applications. (B) Irradiation time-dependent antiviral effects of Mask-TTCP-PF$_6$ with 10^5 $TCID_{50}$/100 μL of H1N1 at a power density of 20 W/m^2 (C–D) Irradiation time-dependent antibacterial effects of Mask-TTCP-PF$_6$ with 10^5 CFU/mL of *Streptococcus pneumoniae* at a power density of 20 W/m^2 (with representative pictures of LB agar plates). (E) Irradiation time-dependent antiviral effects of Mask-TTCP-PF$_6$ with 10^7 $TCID_{50}$/100 μL of H1N1/WSN at a power density of 20 W/m^2 (F–G) Irradiation time-dependent antibacterial effects of Mask-TTCP-PF$_6$ with 10^7 CFU/mL of *S. pneumoniae* at a power density of 20 W/m^2 (with a representative picture of LB agar plates). (H) Irradiation time-dependent antiviral effects of Mask-TTCP-PF$_6$ with 10^7 $TCID_{50}$/100 μL of H1N1 under simulated sunlight. (I–J) Irradiation time-dependent antibacterial effects of Mask-TTCP-PF$_6$ with 10^7 CFU/mL of *S. pneumoniae* under simulated sunlight (with representative pictures of LB agar plates).

characterized. As shown in Fig. 4A, the optical images of Mask-TTCP-PF$_6$ appear pinkish in color, while the blank fabrics appear white. The UV–vis absorption peak at 450 nm appeared in the Mask-TTCP-PF$_6$, which was consistent with the absorption peak of TTCP-PF$_6$ (Figure S4). The microstructure of the Mask-TTCP-PF$_6$ and the original fabric was examined using SEM (Fig. 4B). Unlike the smooth surface of the microfibers of the original fabric, the aggregate with diameter of 255 nm were visible on the surface of the Mask-TTCP-PF$_6$ (Figure S5). These results demonstrated that TTCP-PF$_6$ could easily load on the surface of masks by a simple soaking and drying process, and the simplified process facilitates mass production with low costs. Next, we evaluate the photostability and water stability of Mask-TTCP-PF$_6$ through SEM and ROS generation. The Mask-TTCP-PF$_6$ fabric was exposed to light for 2 h or washed 100 times respectively. After different treatments, TTCP-PF$_6$ remains on the washed or light exposed fabric, similar to the newly prepared Mask-TTCP-PF$_6$ (Fig. 4B, red arrows). Moreover, The Type I and Type II ROS generation ability of Mask-TTCP-PF$_6$ after 2 h of light exposure, and Mask-TTCP-PF$_6$ after 100 times of washing were similar to that of the newly prepared Mask-TTCP-PF$_6$ and higher than the blank one (Fig. 4C, Figure S6). The mentioned results indicate that Mask-TTCP-PF$_6$ has excellent stability with great application prospects.

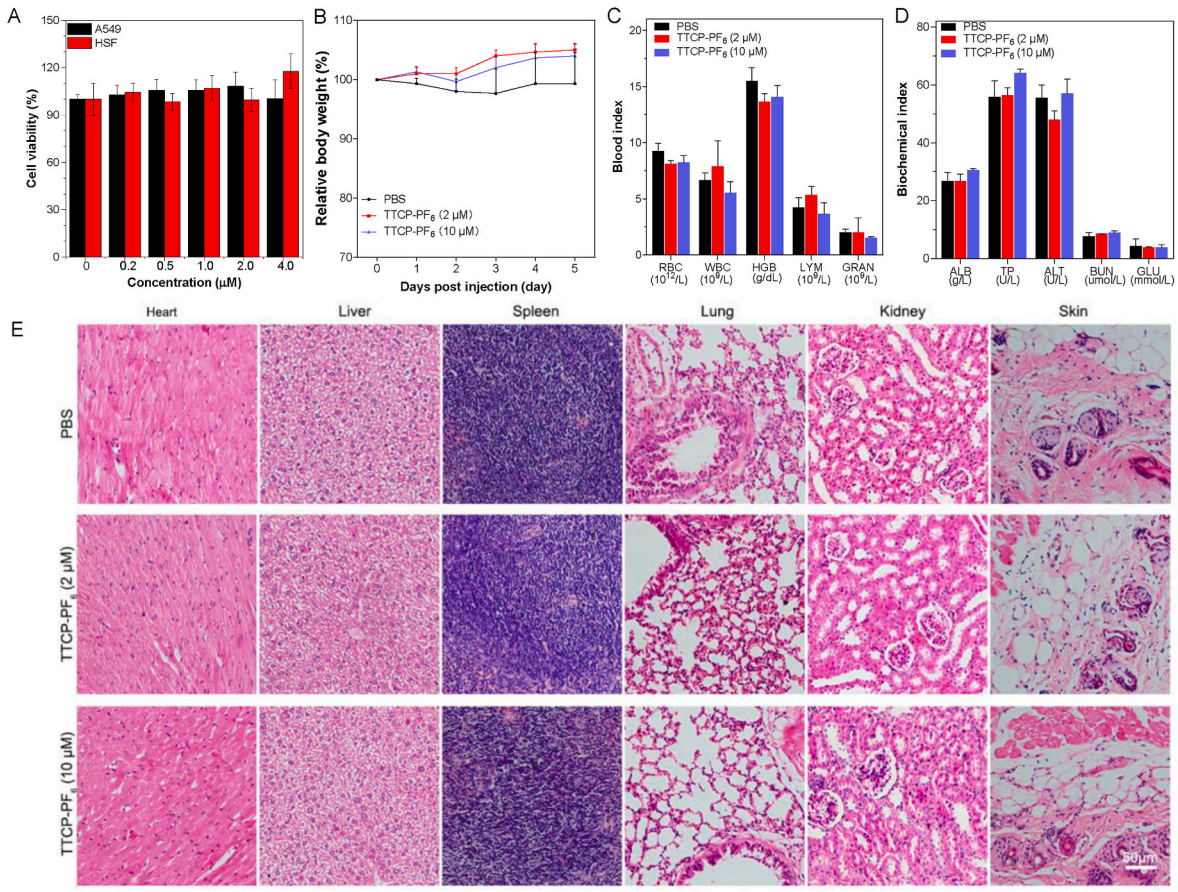

Fig. 6. Biocompatibility evaluation of TTCP-PF$_6$ and Mask-TTCP-PF$_6$. (A) Cell viability of HSF cells and A549 cells after incubation with different concentrations of TTCP-PF$_6$ for 24 h (CCK-8 as the indicator). (B) Body weight changes of ICR mice after intranasal administration of PBS, 2 μM or 10 μM TTCP-PF$_6$ (15 μL). Data were presented as mean ± SEM (n = 3). (C–D) Blood, liver, and kidney function biochemical data of ICR mice 5 days after intranasal administration of PBS, 2 μM or 10 μM TTCP-PF$_6$ (15 μL). Data were presented as mean ± SD (n = 3). (E) Images of various HE-stained organ slices from ICR mice 5 days after intranasally administrated or applied to the skin. Scale bars: 50 μm.

3.3. The light-induced anti-pathogenic effect of mask-TTCP-PF$_6$

Due to the superior anti-pathogenic capability of TTCP-PF$_6$ by ROS generation and the excellent stability of Mask-TTCP-PF$_6$, we then evaluated the actual PDI effect of Mask-TTCP-PF$_6$ intending to fabricate self-cleaning bioprotective masks. A model shown in Fig. 5A was developed to simulate the exposure to pathogens when wearing masks daily. The spraying process simulates the discharge of pathogens by the infectious respiratory fluids, while the vacuum pump simulates the breathing inhalation of the wearer. To explore whether Mask-TTCP-PF$_6$ exhibit a rapid anti-pathogenic ability similar to that of TTCP-PF$_6$ alone under ultra-low-power light irradiation, the power density of light irradiation was fixed at 20 W/m^2. When different concentrations of aerosolized H1N1/WSN or *S. pneumoniae* reached the surface of Mask-TTCP-PF$_6$, Mask-TTCP-PF$_6$ was immediately exposed to the white light of 20 W/m^2 for different durations. The deposited pathogens after different treatments were washed off from the Mask-TTCP-PF$_6$ for quantification. The viral titers of H1N1/WSN were detected through TCID$_{50}$, and the relative bacterial viability of *S. pneumoniae* was analyzed through colony-forming units. As shown in Fig. 5B, more than 90% of H1N1/WSN were significantly inhibited at 10^5 TCID$_{50}$/100 μL after 10 min of 20 W/m^2 light irradiation. More than 85% of the virus was inhibited at 10^7 TCID$_{50}$/100 μL (Fig. 5E). A similar effect was found on *S. pneumoniae* illustrated in Fig. 5C–D and Fig. 5F-G with 10^5 CFU/mL, or even 10^7 CFU/mL of *S. pneumoniae* were completely inhibited with 20 W/m^2 light irradiation for 10 min.

Encouraged by the preceding results, the use of sunlight for the inactivation of pathogens on Mask-TTCP-PF$_6$ was then investigated. Since H1N1/WSN and *S. pneumoniae* require operation in a biosafety level-2 laboratory, we utilized simulated sunlight irradiation as a light source instead of the sun. We found that the Mask-TTCP-PF$_6$ exhibited excellent anti-pathogenic effects, including H1N1 (Fig. 5H) and *S. pneumoniae* (Fig. 5I and J), under simulated sunlight irradiation compared to the blank control masks. 10^7 TCID$_{50}$/100 μL of H1N1/WSN or 10^7 CFU/mL of *S. pneumoniae* were completely inhibited when illuminated with simulated sunlight for 15min and 10 min, respectively. Mask-TTCP-PF$_6$ showed effective anti-pathogenic capability under simulated sunlight, which not only acts as a physical barrier to block pathogens but also eliminates them. Altogether, the results provide a theoretical basis for manufacturing self-cleaning masks.

3.4. Biocompatibility evaluation of TTCP-PF$_6$ and mask-TTCP-PF$_6$

In vitro and in vivo toxicity, as well as the biocompatibility of TTCP-PF6 and Mask-TTCP-PF6 was studied next. Normal cells (A549 and HSF) were first treated with different concentrations of TTCP-PF$_6$ for 24 h, and their cell viability was measured by the CCK-8 assay. As shown in Fig. 6A, the cell viability did not decrease regardless of the concentrations of TTCP-PF$_6$ used (up to 4 μM), confirming that TTCP-PF$_6$ has minimal cytotoxicity to normal lung and skin cells. To evaluate in vivo toxicity of TTCP-PF$_6$, different concentrations of TTCP-PF$_6$ (2 μM or 10 μM) were intranasally administrated or applied to the skin of healthy mice. Mice were kept under conventional laboratory conditions without taking measures to avoid light. Any changes in body weight,

biochemical indexes, and organ damage were recorded. Fig. 6B and S9 showed no noticeable body weight loss in mice compared to the PBS-treated group. Additionally, no changes in the blood index were observed, including red blood cell count (RBC), white blood cell count (WBC), hemoglobin (HGB), lymphocyte (LYM), and neutrophile granulocyte (GRAN). The biochemical indexes, including albumin (ALB), total protein (TP), alanine transaminase (ALT), blood urea nitrogen (BUN), and glucose (GLU) also showed no changes after TTCP-PF_6 treatment (Fig. 6C and D). The analyses indicated no apparent systemic inflammation and dysfunction in the liver and kidney caused by TTCP-PF_6. Other indicators are shown in Tables S1 and S2. Furthermore, HE staining of lungs, skin and other vital organs revealed no pathological changes after TTCP-PF_6 administration for 5 days (Fig. 6E). These results demonstrate that TTCP-PF_6 is a safe biomaterial without toxicity to healthy mice.

4. Conclusion

In summary, we have prepared a self-cleaning mask based on a high-performance aggregation-induced emission photosensitizer (TTCP-PF_6) for pathogen elimination by generating type I and type II reactive oxygen species. The self-cleaning mask has been developed through a simple soaking and drying process. The Mask-TTCP-PF_6 is a sunlight-triggered photodynamic anti-pathogenic fabric against a wide range of pathogens, including bacteria and viruses. When droplets with H1N1/WSN or *S. pneumoniae* get deposited on Mask-TTCP-PF_6, the substantial quantity of ROS produced rapidly inactivates the pathogen upon 10 min of ultra-low powered (20 W/m^2) white light or simulated sunlight irradiation, resulting in self-cleaning without additional equipment. This TTCP-PF_6-based mask can combat airborne pathogens and has a significant potential to avoid re-transmission and re-proliferation of pathogenic microbes as well as to reduce environmental pollution associated with the disposal of large quantities of single-use masks.

Credit author statement

Jingxuan Sun, Yujie Bai and Eric Y. Yu contributed equally to this work. Jingxuan Sun: Conceptualization, methodology, bio-experiments, formal analysis, data curation, writing-original draft. Yujie Bai: Investigation, methodology, in-vivo experiments, formal analysis, data curation, writing-Review & Editing. Eric Y. Yu: chemical experiments, formal analysis, data curation, writing-Review & Editing. Ming Duan and Haili Zhang: resources and methodology. Guanyu Ding, Pei Huang, Mengyao Zhang, and Hongli Jin: methodology, bio-experiments, formal analysis, data curation and discussion. Ryan TK Kwok: writing-Review & Editing. Yuanyuan Li, Guo-Gang Shan, Ben Zhong Tang and Hualei Wang: Conceptualization, methodology, formal analysis, data curation, writing-Review & Editing.

Declaration of competing interest

The authors declare that they have no known competing financial interests or personal relationships that could have appeared to influence the work reported in this paper.

Data availability

Data will be made available on request.

Acknowledgement

This work was supported by the National Key Research and Development Program of China (2021YFC2600202), the National Natural Science Foundation of China (32102642 and 22175033), the Innovation and Technology Commission (ITC-CNERC14SC01), and Research Grant Council of Hong Kong (16306620 and 16303221).

Appendix A. Supplementary data

Supplementary data related to this article can be found at https://doi.org/10.1016/j.biomaterials.2022.121898.

References

[1] B. Diao, K. Wen, J. Zhang, J. Chen, C. Han, Y. Chen, et al., Accuracy of a nucleocapsid protein antigen rapid test in the diagnosis of SARS-CoV-2 infection, Clin. Microbiol. Infect. 27 (2) (2021) 289.e1–289.e4.
[2] R. Lu, X. Zhao, J. Li, P. Niu, B. Yang, H. Wu, et al., Genomic characterisation and epidemiology of 2019 novel coronavirus: implications for virus origins and receptor binding, Lancet 395 (10224) (2020) 565–574.
[3] J.M. Sharfstein, S.J. Becker, M.M. Mello, Diagnostic testing for the novel coronavirus, JAMA 323 (15) (2020) 1437–1438.
[4] C. Sohrabi, Z. Alsafi, N. O'Neill, M. Khan, A. Kerwan, A. Al-Jabir, et al., World health organization declares global emergency: a review of the 2019 novel coronavirus (COVID-19), Int. J. Surg. 76 (2020) 71–76.
[5] A. Telenti, A. Arvin, L. Corey, D. Corti, M.S. Diamond, A. García-Sastre, et al., After the pandemic: perspectives on the future trajectory of COVID-19, Nature 596 (7873) (2021) 495–504.
[6] J. Bedford, D. Enria, J. Giesecke, D.L. Heymann, C. Ihekweazu, G. Kobinger, et al., COVID-19: towards controlling of a pandemic, Lancet 395 (10229) (2020) 1015–1018.
[7] W.J. Wiersinga, A. Rhodes, A.C. Cheng, S.J. Peacock, H.C. Prescott, Pathophysiology, transmission, diagnosis, and treatment of coronavirus disease 2019 (COVID-19): a review, JAMA 324 (8) (2020) 782–793.
[8] Y.Y. Zuo, W.E. Uspal, T. Wei, Airborne transmission of COVID-19: aerosol dispersion, lung deposition, and virus-receptor interactions, ACS Nano (2020) 16502–16524.
[9] M.H. Chua, W. Cheng, S.S. Goh, J. Kong, B. Li, J.Y.C. Lim, et al., Face masks in the new COVID-19 normal: materials, testing, and perspectives, Research 2020 (2020), 7286735.
[10] M. Karmacharya, S. Kumar, O. Gulenko, Y.K. Cho, Advances in facemasks during the COVID-19 pandemic era, ACS Appl. Bio Mater. 4 (5) (2021) 3891–3908.
[11] S. Feng, C. Shen, N. Xia, W. Song, M. Fan, B.J. Cowling, Rational use of face masks in the COVID-19 pandemic, Lancet Respir. Med. 8 (5) (2020) 434–436.
[12] L. Huang, S. Xu, Z. Wang, K. Xue, J. Su, Y. Song, et al., Self-reporting and photothermally enhanced rapid bacterial killing on a laser-induced graphene mask, ACS Nano 14 (9) (2020) 12045–12053.
[13] L. Huang, M. Gu, Z. Wang, T.W. Tang, Z. Zhu, Y. Yuan, et al., Highly efficient and rapid inactivation of coronavirus on non-metal hydrophobic laser-induced graphene in mild conditions, Adv. Funct. Mater. 31 (24) (2021), 2101195.
[14] H. Zhong, Z. Zhu, P. You, J. Lin, C.F. Cheung, V.L. Lu, et al., Plasmonic and superhydrophobic self-decontaminating n95 respirators, ACS Nano 14 (7) (2020) 8846–8854.
[15] G. Jori, S.B. Brown, Photosensitized inactivation of microorganisms, Photochem. Photobiol. Sci. 3 (5) (2004) 403–405.
[16] A.B. Ormond, H.S. Freeman, Dye sensitizers for photodynamic therapy, Materials 6 (3) (2013) 817–840.
[17] M. Wainwright, Photoinactivation of viruses, Photochem. Photobiol. Sci. 3 (5) (2004) 406–411.
[18] A. Wiehe, J.M. O'Brien, M.O. Senge, Trends and targets in antiviral phototherapy, Photochem. Photobiol. Sci. 18 (11) (2019) 2565–2612.
[19] F. Cieplik, D. Deng, W. Crielaard, W. Buchalla, E. Hellwig, A. Al-Ahmad, et al., Antimicrobial photodynamic therapy - what we know and what we don't, Crit. Rev. Microbiol. 44 (5) (2018) 571–589.
[20] H. Li, M. Yang, J.S. Kim, J. Ha, J. Han, H. Kim, et al., Structure-oriented design strategy to construct nir aiegens to selectively combat gram (+) multidrug-resistant bacteria in vivo, Biomaterials 286 (2022), 121580.
[21] D.B. Zorov, M. Juhaszova, S.J. Sollott, Mitochondrial reactive oxygen species (ros) and ros-induced ros release, Physiol. Rev. 94 (3) (2014) 909–950.
[22] B.L. Carpenter, F. Scholle, H. Sadeghifar, A.J. Francis, J. Boltersdorf, W.W. Weare, et al., Synthesis, characterization, and antimicrobial efficacy of photomicrobicidal cellulose paper, Biomacromolecules 16 (8) (2015) 2482–2492.
[23] Y. Lhotáková, L. Plíštil, A. Morávková, P. Kubát, K. Lang, J. Forstová, et al., Virucidal nanofiber textiles based on photosensitized production of singlet oxygen, PLoS One 7 (11) (2012), e49226.
[24] M.T. Jarvi, M.J. Niedre, M.S. Patterson, B.C. Wilson, The influence of oxygen depletion and photosensitizer triplet-state dynamics during photodynamic therapy on accurate singlet oxygen luminescence monitoring and analysis of treatment dose response, Photochem. Photobiol. 87 (1) (2011) 223–234.
[25] J.R. Kanofsky, Measurement of singlet-oxygen in vivo: progress and pitfalls, Photochem. Photobiol. 87 (1) (2011) 14–17.
[26] M. Garcia-Diaz, Y.Y. Huang, M.R. Hamblin, Use of fluorescent probes for ros to tease apart type i and type ii photochemical pathways in photodynamic therapy, Methods 109 (2016) 158–166.
[27] M. Li, H. Wen, H. Li, Z.-C. Yan, Y. Li, L. Wang, et al., AIEgen-loaded nanofibrous membrane as photodynamic/photothermal antimicrobial surface for sunlight-triggered bioprotection, Biomaterials 276 (2021), 121007.
[28] Z. Liu, Q. Wang, W. Qiu, Y. Lyu, Z. Zhu, X. Zhao, et al., Aie-active luminogens as highly efficient free-radical ros photogenerator for image-guided photodynamic therapy, Chem. Sci. 13 (12) (2022) 3599–3608.

[29] V. Saini, V. Venkatesh, Aie material for photodynamic therapy, Prog Mol Biol Transl Sci 185 (2021) 45–73.
[30] W. Zhai, Y. Zhang, M. Liu, H. Zhang, J. Zhang, C. Li, Universal scaffold for an activatable photosensitizer with completely inhibited photosensitivity, Angew Chem. Int. Ed. Engl. 58 (46) (2019) 16601–16609.
[31] S. Wang, X. Wang, L. Yu, M. Sun, Progress and trends of photodynamic therapy: from traditional photosensitizers to aie-based photosensitizers, Photodiagnosis Photodyn. Ther. 34 (2021), 102254.
[32] W. Wu, D. Mao, F. Hu, S. Xu, C. Chen, C.J. Zhang, et al., A highly efficient and photostable photosensitizer with near-infrared aggregation-induced emission for image-guided photodynamic anticancer therapy, Adv. Mater. 29 (33) (2017).
[33] S. Xu, Y. Duan, B. Liu, Precise molecular design for high-performance luminogens with aggregation-induced emission, Adv. Mater. 32 (1) (2020), e1903530.
[34] W. Xu, M.M.S. Lee, Z. Zhang, H.H.Y. Sung, I.D. Williams, R.T.K. Kwok, et al., Facile synthesis of aiegens with wide color tunability for cellular imaging and therapy, Chem. Sci. 10 (12) (2019) 3494–3501.
[35] C. Pan, W. Zhao, X. Zhao, Z. Liu, X. Li, Y. Lyu, et al., Type I Photosensitizer Based on Aie Chromophore Tricyano-Methylene-Pyridine for Photodynamic Therapy, Green Ch E, 2022, https://doi.org/10.1016/j.gce.2022.07.004.
[36] S. Xu, Y. Yuan, X. Cai, C.J. Zhang, F. Hu, J. Liang, et al., Tuning the singlet-triplet energy gap: a unique approach to efficient photosensitizers with aggregation-induced emission (aie) characteristics, Chem. Sci. 6 (10) (2015) 5824–5830.
[37] L. Yang, X. Wang, G. Zhang, X. Chen, G. Zhang, J. Jiang, Aggregation-induced intersystem crossing: a novel strategy for efficient molecular phosphorescence, Nanoscale 8 (40) (2016) 17422–17426.
[38] M. Li, Y. Gao, Y. Yuan, Y. Wu, Z. Song, B.Z. Tang, et al., One-step formulation of targeted aggregation-induced emission dots for image-guided photodynamic therapy of cholangiocarcinoma, ACS Nano 11 (4) (2017) 3922–3932.
[39] Y. Liao, B. Li, Z. Zhao, Y. Fu, Q. Tan, X. Li, et al., Targeted theranostics for tuberculosis: a rifampicin-loaded aggregation-induced emission carrier for granulomas tracking and anti-infection, ACS Nano 14 (7) (2020) 8046–8058.
[40] K. Han, S.B. Wang, Q. Lei, J.Y. Zhu, X.Z. Zhang, Ratiometric biosensor for aggregation-induced emission-guided precise photodynamic therapy, ACS Nano 9 (10) (2015) 10268–10277.
[41] N. Okahashi, T. Sumitomo, M. Nakata, S. Kawabata, Secondary streptococcal infection following influenza, Microbiol. Immunol. 66 (6) (2022) 253–263.
[42] L.J. Reed, H. Muench, A simple method of estimating fifty per cent endpoints12, Am. J. Epidemiol. 27 (3) (1938) 493–497.
[43] N. Suárez, E. Texeira, Optimal conditions for streptococcus pneumoniae culture: in solid and liquid media, Methods Mol. Biol. 1968 (2019) 3–10.
[44] G. Ding, J. Tong, Y. Duan, S. Wang, Z. Su, K. Shao, et al., Boosting the photodynamic therapy of near-infrared aie-active photosensitizers by precise manipulation of the molecular structure and aggregate-state packing, J. Mater. Chem. B 10 (30) (2022) 5818–5825.
[45] P. Xiao, Z. Shen, D. Wang, Y. Pan, Y. Li, J. Gong, et al., Precise molecular engineering of type i photosensitizers with near-infrared aggregation-induced emission for image-guided photodynamic killing of multidrug-resistant bacteria, Adv. Sci. 9 (5) (2022), e2104079.
[46] G. Yuan, C. Lv, J. Liang, X. Zhong, Y. Li, J. He, et al., Molecular engineering of efficient singlet oxygen generators with near-infrared aie features for mitochondrial targeted photodynamic therapy, Adv. Funct. Mater. 31 (36) (2021), 2104026.
[47] Y.C. Ma, Y.H. Zhu, X.F. Tang, L.F. Hang, W. Jiang, M. Li, et al., Au nanoparticles with enzyme-mimicking activity-ornamented zif-8 for highly efficient photodynamic therapy, Biomater. Sci. 7 (7) (2019) 2740–2748.
[48] S.K. Sharma, M.R. Hamblin, The use of fluorescent probes to detect ros in photodynamic therapy, Methods Mol. Biol. 2202 (2021) 215–229.
[49] M. Yazdani, Concerns in the application of fluorescent probes dcdhf-da, dhr 123 and dhe to measure reactive oxygen species in vitro, Toxicol. Vitro 30 (1 Pt B) (2015) 578–582.
[50] L. Si, H. Xu, X. Zhou, Z. Zhang, Z. Tian, Y. Wang, et al., Generation of influenza a viruses as live but replication-incompetent virus vaccines, Science 354 (6316) (2016) 1170–1173.
[51] X. Wang, J. Xiong, D. Zhou, S. Zhang, L. Wang, Q. Tian, et al., Trim34 modulates influenza virus-activated programmed cell death by targeting z-DNA-binding protein 1 for k63-linked polyubiquitination, J. Biol. Chem. 298 (3) (2022), 101611.
[52] A.J. Lee, A.A. Ashkar, The dual nature of type i and type ii interferons, Front. Immunol. 9 (2018) 2061.
[53] G. Kazdaglis, J. Lucin, K. Kertat, S. Persis, Four methods for identifying ambiguous streptococcus pneumoniae isolates: the experience from a Swedish university hospital, J. Biol. Regul. Homeost. Agents 33 (3) (2019) 843–847.
[54] P.N. Tawakoli, A. Al-Ahmad, W. Hoth-Hannig, M. Hannig, C. Hannig, Comparison of different live/dead stainings for detection and quantification of adherent microorganisms in the initial oral biofilm, Clin. Oral Invest. 17 (3) (2013) 841–850.
[55] R. Nadhan, D. Patra, N. Krishnan, A. Rajan, S. Gopala, D. Ravi, et al., Perspectives on mechanistic implications of ros inducers for targeting viral infections, Eur. J. Pharmacol. 890 (2021), 173621.
[56] L. Tao, A. Lemoff, G. Wang, C. Zarek, A. Lowe, N. Yan, et al., Reactive oxygen species oxidize sting and suppress interferon production, Elife 9 (2020), e57837.
[57] Y. Zhang, Q. Wang, Z. Zhu, W. Zhao, C. Yan, Z. Liu, et al., Spatiotemporal visualization of cell membrane with amphiphilic aggregation-induced emission-active sensor, CCS Chem, 4 (5) (2022) 1619–1632.
[58] J. Huang, B. He, Z. Zhang, Y. Li, M. Kang, Y. Wang, et al., Aggregation-induced emission luminogens married to 2D black phosphorus nanosheets for highly efficient multimodal theranostics, Adv. Mater. 32 (37) (2020), 2003382.